Chapter 2
Ground-Based Aerosol Optical Depth Measurements

Abstract This chapter presents a detailed overview on the theory of aerosol optical depth retrieval with the emphasis on ground-based sunphotometry technique. To further discuss on the calibration issue as mentioned previously, this overview also includes the principle of the oldest passive ground-based calibration method, Langley calibration to provide an insight on the working mechanism of the method. The final part in this chapter compiles the previous existing Langley calibration method in a chronological sequence to render a better comprehension on its development from the past to present time.

Keywords Aerosol optical depth · Sunphotometers · Spectroradiometer · Langley calibration

2.1 Theory of Aerosol Absorption and Scattering

The fundamental theory of aerosol absorption and scattering is explained by Mie theory which describes the attenuation of electromagnetic radiation by spherical particles through solving the Maxwell equations. Mie theory is also called Lorenz-Mie theory or Lorenz-Mie-Debye theory. In this theory, there are two important key assumptions: (1) particle is a sphere, and (2) particle is homogenous and therefore it is characterized by single refractive index $m = n - ik$ at a given wavelength. Mie theory requires the relative refractive index that is the refractive index of a particle divided the refractive index of a medium. In this case, the medium of atmospheric aerosol is often assumed in air of m is about 1 and since it has complex chemical composition, the effective refractive index is often calculated at a given wavelength.

Basically, Mie theory calculates the scattered electromagnetic field at all points within the particle which called internal field and at all points of the homogeneous medium in which the particle is embedded as shown in Fig. 2.1. In almost all practical applications in atmosphere, light scattering observations are carried out in

J. Dayou et al., *Ground-Based Aerosol Optical Depth Measurement Using Sunphotometers*, SpringerBriefs in Applied Sciences and Technology,
DOI: 10.1007/978-981-287-101-5_2, © The Author(s) 2014

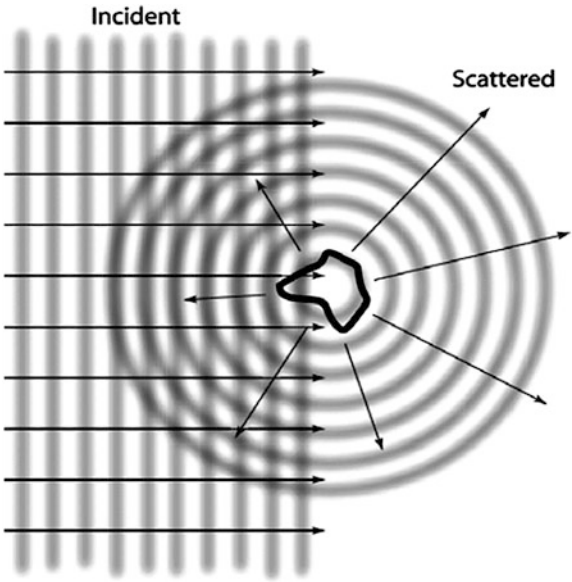

Fig. 2.1 Simplified visualization of scattering of an incident EM wave by particle

the far-field zone (i.e., at the large distances R from a particle). The solution of the wave equation in the far field zone can be obtained as (Mie 1908)

$$\begin{bmatrix} E_l^s \\ E_r^s \end{bmatrix} = \frac{\exp(-ikR + ikI)}{ikR} \begin{bmatrix} S_2(\theta) & S_3(\theta) \\ S_4(\theta) & S_1(\theta) \end{bmatrix} \begin{bmatrix} E_l^i \\ E_r^i \end{bmatrix}, \tag{2.1}$$

where $k = 2\pi/\lambda$, E_l^i and E_r^i are the parallel and perpendicular components of incident electrical field, and E_l^s and E_r^s are the parallel and perpendicular components of scattered electrical field, $\begin{bmatrix} S_2(\theta) & S_3(\theta) \\ S_4(\theta) & S_1(\theta) \end{bmatrix}$ is the amplitude scattering matrix at scattering angle θ.

As the first assumption suggested, for spherical particle, $S_3(\theta)$ and $S_4(\theta)$ are zero, and thus Eq. 2.1 gives the fundamental equation of scattered radiation by a sphere including polarization as

$$\begin{bmatrix} E_l^s \\ E_r^s \end{bmatrix} = \frac{\exp(-ikR + ikI)}{ikR} \begin{bmatrix} S_2(\theta) & 0 \\ 0 & S_1(\theta) \end{bmatrix} \begin{bmatrix} E_l^i \\ E_r^i \end{bmatrix}. \tag{2.2}$$

In Eq. 2.2, the Mie theory defines scattering amplitudes $S_1(\theta)$ and $S_2(\theta)$ function as (Mie 1908)

$$S_1(\theta) = \sum_{n=1}^{\infty} \frac{2n+1}{n(n+1)} [a_n \pi_n(\cos\theta) + b_n \tau_n(\cos\theta)], \tag{2.3}$$

$$S_2(\theta) = \sum_{n=1}^{\infty} \frac{2n+1}{n(n+1)} [b_n \pi_n(\cos\theta) + a_n \tau_n(\cos\theta)], \tag{2.4}$$

where $\pi_n(\cos\theta)$ and $\tau_n(\cos\theta)$ are Mie angular functions written as

$$\pi_n(\cos\theta) = \frac{1}{\sin(\theta)} P_n^1(\cos\theta), \tag{2.5}$$

$$\tau_n(\cos\theta) = \frac{d}{d\theta} P_n^1(\cos\theta), \tag{2.6}$$

where P_n^1 are the associated Legendre polynomials, a_n and b_n are scattering coefficient in the function of size parameter x.

To determine the scattering phase function P_n^1 $(\cos\theta)$, Mie theory relates the Stoke parameters $\{I_o, Q_o, V_o, U_o\}$ of incident radiation field and Stoke parameters $\{I, Q, V, U\}$ of scattered radiation as (Bohren and Huffman 1983)

$$\begin{bmatrix} I \\ Q \\ V \\ U \end{bmatrix} = \frac{\sigma_s}{4\pi r^2} P \begin{bmatrix} I_o \\ Q_o \\ V_o \\ U_o \end{bmatrix}, \tag{2.7}$$

where P is defined as

$$P = \begin{bmatrix} P_{11} & P_{12} & 0 & 0 \\ P_{12} & P_{22} & 0 & 0 \\ 0 & 0 & P_{33} & -P_{34} \\ 0 & 0 & P_{34} & P_{44} \end{bmatrix}. \tag{2.8}$$

In a particle of any shape, the scattering phase function consists of 16 independent elements, but for a spherical particle this number reduces to four as $P_{22} = P_{11}$, $P_{44} = P_{33}$. Thus, for sphere, Eq. 2.7 is rewritten as

$$\begin{bmatrix} I \\ Q \\ V \\ U \end{bmatrix} = \frac{\sigma_s}{4\pi r^2} \begin{bmatrix} P_{11} & P_{12} & 0 & 0 \\ P_{12} & P_{11} & 0 & 0 \\ 0 & 0 & P_{33} & -P_{34} \\ 0 & 0 & P_{34} & P_{33} \end{bmatrix} \begin{bmatrix} I_o \\ Q_o \\ V_o \\ U_o \end{bmatrix}. \tag{2.9}$$

where σ_s and r are the scattering cross-section and radius of the particle respectively.

From Mie theory, it is given that the extinction cross-section of a particle with radius r in the forward direction $\theta = 0°$ as (Bohren and Huffman 1983)

$$\sigma_s = \frac{4\pi}{k^2}\mathrm{Re}[S(\theta = 0^\circ)]. \tag{2.10}$$

Following Eqs. 2.3 and 2.4 in $\theta = 0°$, both equations yield

$$S_1(0^\circ) = S_2(0^\circ) = \frac{1}{2}\sum_{n=1}^{\infty}(2n+1)(a_n + b_n). \tag{2.11}$$

The efficiencies Q of extinction, scattering, absorption are defined as

$$Q = \frac{\sigma}{\pi r^2}, \tag{2.12}$$

where σ is the cross-section of a particle with radius r. This brings the solution for Q_e. Q_s, and Q_a in terms coefficents a_n and b_n as

$$Q_e = \frac{2}{x^2}\sum_{n=1}^{\infty}(2n+1)\mathrm{Re}(a_n + b_n), \tag{2.13}$$

$$Q_s = \frac{2}{x^2}\sum_{n=1}^{\infty}(2n+1)(|a_n|^2 + |b_n|^2), \tag{2.14}$$

$$Q_a = Q_e - Q_s, \tag{2.15}$$

where x is the size parameter.

2.1.1 The Optical Properties of Spherical Particle

In the previous section, Mie theory was used to define the extinction, scattering, and absorption cross-section as a function of particle size and wavelength. In this section, the cross section of extinction, scattering, and absorption is integrated over the size distribution *N(r)* to yield the optical properties of an ensemble spherical particle.

For a given type of particles characterized by the size distribution *N(r)dr*, the volume extinction K_e, scattering K_s and absorption K_a coefficients are determined as (King et al. 1978)

$$K_e = \int_{r_1}^{r_2}\sigma_e(r)N(r)dr = \int_{r_1}^{r_2}\pi r^2 Q_e N(r)dr; \tag{2.16}$$

$$K_s = \int_{r_1}^{r_2}\sigma_s(r)N(r)dr = \int_{r_1}^{r_2}\pi r^2 Q_s N(r)dr; \tag{2.17}$$

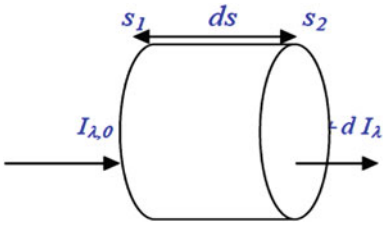

Fig. 2.2 Intrinsic visualisation of transmission of an extraterrestrial radiation $I_{\lambda,o}$ through an optical path length s_1 and s_2

$$K_a = \int_{r_1}^{r_2} \sigma_a(r) N(r) dr = \int_{r_1}^{r_2} \pi r^2 Q_a N(r) dr. \tag{2.18}$$

On the other hand, for external mixture that contains several types of particles, the total effective volume extinction, scattering and absorption are the sum of each particle component as

$$K_e = \sum_i K_e^i = \sum_i \int_{r_1}^{r_2} \sigma_e(r) N_i(r) dr = \sum_i \int_{r_1}^{r_2} \pi r^2 Q_e N_i(r) dr, \tag{2.19}$$

$$K_s = \sum_i K_s^i = \sum_i \int_{r_1}^{r_2} \sigma_s(r) N_i(r) dr = \sum_i \int_{r_1}^{r_2} \pi r^2 Q_s N_i(r) dr, \tag{2.20}$$

$$K_a = \sum_i K_a^i = \sum_i \int_{r_1}^{r_2} \sigma_a(r) N_i(r) dr = \sum_i \int_{r_1}^{r_2} \pi r^2 Q_a N_i(r) dr, \tag{2.21}$$

where K_e^i, K_s^i, and K_a^i are calculated for each particle type characterized by its particle size distribution $N_i(r)$ and a refractive index m_i.

On the whole, the fundamental theory of Mie particle scattering and absorption resulted in the main radiation law of extinction which also known as Beer-Lambert-Bouger's Law. It states that the extinction process is linear in the intensity of radiation and amount of matter, provided that the physical state (i.e., temperature, pressure, composition) is held constant. Consider a small volume ΔV of infinitesimal length ds and unit area ΔA containing optically active matter (gases, aerosols, and/or cloud drops) as shown in Fig. 2.2. The change of intensity along a path ds of a light with wavelength λ is proportional to the amount of matter in the path as

$$dI_\lambda = -K_{e,\lambda} I_{\lambda,o} ds, \tag{2.22}$$

where $K_{e,\lambda}$ is the volume extinction coefficient obtained from Eq. 2.19 and, $I_{\lambda,o}$ is the source of function which in this case is the extraterrestrial solar radiation at zero air mass. The optical depth of a specific layer between s_1 and s_2 is then determined by integrating Eq. 2.22 in optical path s as (Dubovik and King 2000)

$$\tau_{\lambda(s_1,s_2)} = \int_{S_1}^{S_2} K_{e,\lambda} ds. \tag{2.23}$$

Finally, it leads to the well-known Beer-Lambert-Bouger's Law of extinction as

$$I_\lambda = I_{\lambda,o} \exp\left(\int_{s_1}^{s_2} -K_{e,\lambda} ds\right) = I_{\lambda,o} \exp(-\tau_\lambda). \tag{2.24}$$

2.2 Ground-Based Aerosol Optical Depth Retrieval

The two most well-known ground-based AOD retrieval techniques are sunphotometry and lidar. The former is a passive optical system that measures the extinction of direct-beam radiation in distinct wavelengths, and retrieves the aerosol contribution to the total extinction. The latter is an active optical system transmits light into the atmosphere and then collects the backscatter light signals to retrieve the aerosol attenuation in total columnar atmosphere. Details of each technique are separately discussed in the following sub-sections.

2.2.1 Retrieval with Ground-Based Sunphotometry Radiometer

Unlike the satellite data that uses upwelling radiances viewed from space, ground-based sunphotometry radiometer uses the down-welling radiances of solar radiation to retrieve total columnar AOD in a specific area. Under cloudless condition, the higher the extinction value in the solar transmission corresponds to higher aerosol loading. Figure 2.3 demonstrates this effect for increasing AOD from 0 to 1 at constant air mass (AM1.5). The blue line at the top represents the extraterrestrial solar spectrum at zero air mass (AM0), which is considered as aerosol-free spectrum. The solar spectrum in direct normal irradiance (DNI) gradually decreases for increasing AOD due to scattering and absorption caused atmospheric aerosols for all wavelengths. From the figure, it is obvious that higher attenuation is experienced by light in the mid-visible range of the solar spectrum compared to other parts of the spectrum. This explains why in most aerosol measurements, visible range wavelengths are regularly used for spectral AOD retrieval. To provide an overview of the ground-based sunphotometry measurement, a number of selected aerosol monitoring networks including Aerosol Robotic Network (AERONET), Multi-Filter Rotating Shadowband Radiometer (MFRSR), China Meteorological Administration Aerosol Remote Sensing Network (CASRNET), and Maritime Aerosol Network (MAN) are briefly discussed as follows.

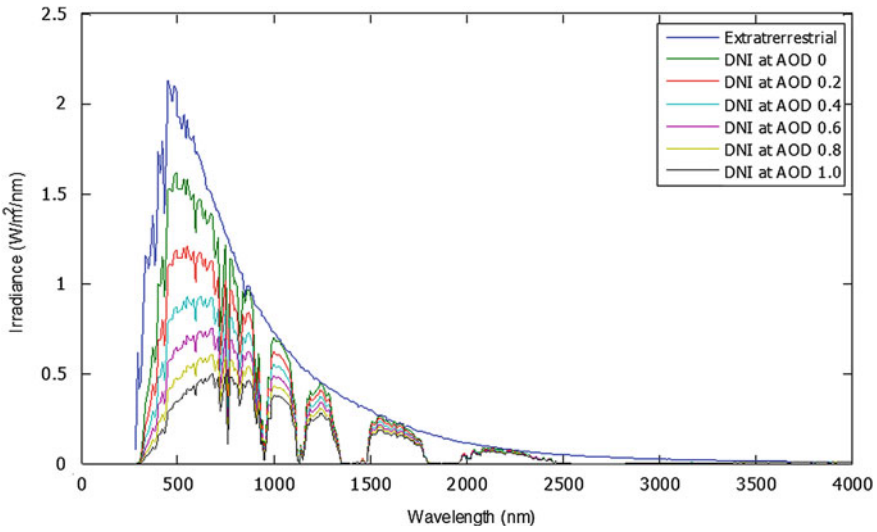

Fig. 2.3 Diminution of solar transmission at multiple AOD values from 0 to 1. Simulation is based on urban aerosol model over tropical atmosphere

2.2.1.1 Aerosol Robotic Network (AERONET)

At global scale over land, AOD is monitored by AERONET project, a federation of ground-based remote sensing aerosol networks established by National Aeronautics and Space Administration (NASA) and PHysics, Optoelectronics, and Technology of Novel Micro-resonator Structures (PHOTONS). It is greatly expanded by collaborators from national agencies, institutes, universities, and individual scientist with currently over 120 monitoring stations across the world, but this does not provide global coverage as illustrated in the map shown in Fig. 2.4. It uses sun photometer CIMEL CE-318 to retrieve AOD within the spectral range 340–1020 nm by means a filtered detector that measures the spectral extinction of direct beam radiation according to Beer-Lambert-Bouguer's Law.

Approximately every 15 min, the sunphotometer points directly at the sun during the daytime, taking spectral measurements in triplicate over 1.5 min. Cloud-screening algorithm is performed by limiting the variability within each triplet and compared to prior and subsequent triplets (Smirnov et al. 2000). Estimates of Angstrom's exponent, and separation into fine and coarse mode contributions, can also be computed via the spectral de-convolution algorithm of O'Neill et al. (2001). Despite the direct sun measurements, AERONET instruments are also programmed to observe angular distribution of sky radiance in approximately every hour during the daytime. These sky measurements are used to retrieve size distribution and scattering/extinction properties of the ambient aerosol using spherical aerosol assumptions (Dubovik and King 2000). By assuming the ambient aerosol to be polydisperse spheres and randomly oriented spheroids, the algorithm

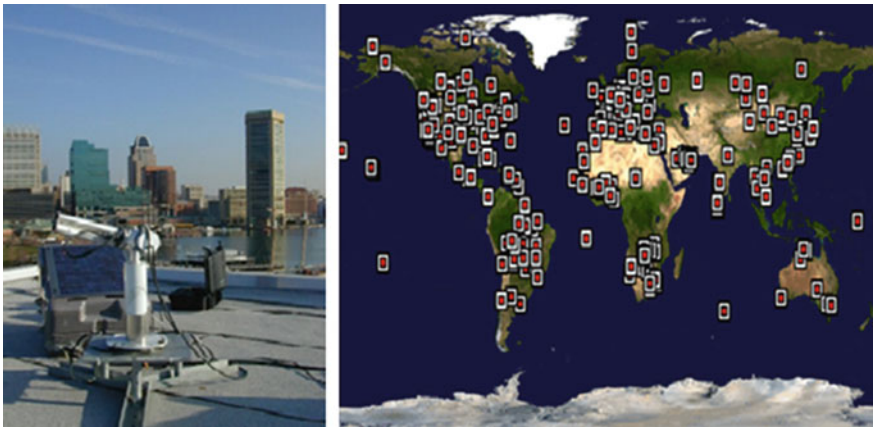

Fig. 2.4 AERONET networks worldwide and CIMEL sunphotometer—adapted from AERONET NASA in http://aeronet.gsfc.nasa.gov/

retrieves the volume distribution that corresponds to the best fit of both sun-measured AOD and sky radiances.

Retrievals from both sun and sky AERONET measurements are controlled by rigorous calibration and cloud-screening algorithms. Limitations of the retrieval also relate to low optical depth conditions, angular coverage of sky radiance measurements, and azimuth angle pointing of the instrument (Dubovik et al. 2000). Nevertheless, it is expected that precise aerosol characterization in the absorption and optical properties could yield accurate retrieval results that can be used as ground-truth estimates (Dubovik et al. 2002).

2.2.1.2 Multifilter Rotating Shadowband Radiometer Network

Ground-based aerosol monitoring network is also supplemented by multifilter rotating shadowband radiometer (MFRSR) networks which measure total and diffuse solar irradiances at multiple wavelengths using shadowband technique. Instead of using the narrow field-of-view (FOV) approximation, direct solar irradiance is obtained by subtracting the diffuse radiation from the total irradiance. This new robotic instruments are mostly operated in remote areas over United States and usually unattended (Augustine et al. 2003). Thus, their raw data represent wide range of atmospheric condition, which are undesirable for AOD retrieval, especially when clouds obscure the sun. Currently, the network uses independent cloud screening algorithm to filter the data suitable for spectral AOD retrieval (Alexandrov et al. 2004). The proposed algorithm characterizes the degree of horizontal inhomogeneity of an atmospheric field. It provides computational efficiency and the ability to detect short clear sky intervals under broken cloud cover conditions.

Furthermore, most MFRSRs are not calibrated against standard references but calibrated in a relative sense from their own operational data (Augustine et al. 2003). The usual calibration method used is Langley plot technique, in which the instrument's output at TOA is inferred by extrapolating to zero air mass. Once a stable extrapolated value is obtained, it can be used for AOD retrieval within the calibration period.

2.2.1.3 China Meteorological Administration Aerosol Remote Sensing Network

In China, it has its own aerosol monitoring program called China Meteorological Administration Aerosol Remote Sensing Network (CARSNET), established in 2002 (Che et al. 2009). It is a routine operation network, purposely launched for the study of aerosol properties and for validation of satellite aerosol retrievals. Similar to AERONET, it deploys the CIMEL sunphotometer for the measurement of direct spectral solar radiance. The CARSNET sunphotometer is annually calibrated to ensure its performance and quality of measurements.

CARSNET has established an independent calibration system that is consistent to AERONET (Che et al. 2009). It uses two master instruments to inter-calibrate all other instruments of the network. The two masters are calibrated by the Langley method following the AERONET protocols in Izana Observatory. In order to contain the uncertainty caused by the degradation of the instruments themselves, the two master instruments of CARSNET are calibrated periodically every three or six months at Waliguan Mountain (36 °17'N, 100 °55'E, 3816 m) the Global Atmosphere Watch (GAW) station of China alternately.

2.2.1.4 Maritime Aerosol Network

To extend the aerosol monitoring over ocean, Maritime Aerosol Network (MAN) as a component of AERONET has been established since November 2006. MAN employs the Microtops handheld sunphotometer and utilizes calibration and data processing procedures traceable to AERONET. A valid comparison among various models, satellite products and sunphotometer measurement suggested that majority of the AOD differences are positive by a factor of 0.2 at most (Smirnov et al. 2011). The discrepancy is believed to be, at least partly, by uncertainties in aerosol production rates, foam formation and its latitudinal distribution, cloud contamination, accuracy of radiative transfer model used, surface reflectance effects.

2.3 Conventional Langley Calibration Method

This section explains the principle of the oldest passive ground-based calibration method, Langley calibration. Until now, the stated method is widely used in many AOD monitoring networks because it requires no additional calibration equipments. However, its accuracy is strongly governed by the atmospheric condition where the calibration is performed. For an ideal condition, it is often performed at high altitude to avoid abundant cloud cover and high unstable aerosol content.

The Langley method uses the changes of observed path length through the atmosphere to compute an optical depth (Harrison and Michalsky 1994). It is a method to measure the sun's irradiances with ground-based instruments that based on repeated measurements operated at a given location for a cloudless morning or afternoon, as the sun moves across the sky for significant changes of air mass or path length. A successful Langley plot is imperative to permit extrapolation of the regression line to air mass zero. The extrapolated value further allows the determination of the instrument output at top of atmosphere or better known as extraterrestrial value. This value is then useful in radiometric calibration when divided by spectrally extraterrestrial irradiances constant (Nieke et al. 1999; Schmid and Wherli 1994). It can also be used in aerosol optical depth retrieval when divided with solar irradiances measured at ground after subtractions by other relevant optical depths.

Figure 2.5 presents an idealized Langley plot at 500 nm for different AOD values from 0.02 to 0.30. It should be noted that no specific reason is inherited in the negative values of irradiance in the y-axis, as value of <1 produces negative natural logarithm. From the figure, it clearly shows that extrapolation to zero air mass by Langley plot for AOD 0.02–0.10 gives a nearly consistent extraterrestrial constant, though with some negligible errors. However, when under high aerosol content (refer line AOD 0.20 and 0.30 in Fig. 2.5), the extrapolation could incur serious inaccuracy even for highly stable aerosol content. Therefore, this leads to believe that for an ideal performance of Langley plot at any wavelengths, a highly stable and low in magnitude aerosol loading is of necessary important.

Its working principle lies on the basis that as the solar radiation transmits through atmosphere, it experiences a stream of attenuations either by absorption or scattering due to the air molecules or solid particles suspended in the atmosphere. From Eq. 2.24, the attenuation of an electromagnetic radiation through an optical path length can be described by the Beer-Lambert-Bougeur's Law. By applying the fundamental theory of Mie scattering and absorption in Sun's direct-beam monochromatic radiation passing through the Earth's atmosphere, it obeys the extinction law of exponential as (Thomason et al. 1983)

$$I_\lambda = R^2 I_{o,\lambda} \exp\left(-\sum \tau_{\lambda,i} m_i\right) \tag{2.25}$$

where I_λ is the direct normal irradiance at the ground at wavelength λ, R is the Earth-to-Sun distance in astronomical units (AU), $I_{o,\lambda}$ is the extraterrestrial

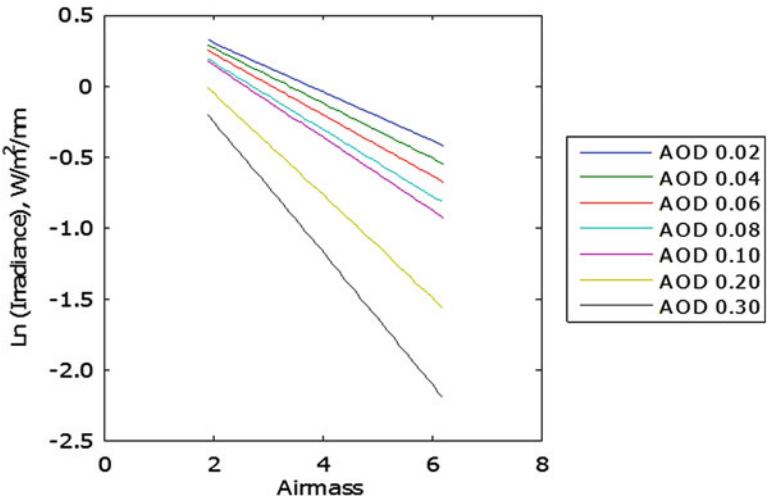

Fig. 2.5 Idealized Langley plot at 500 nm for multiple AOD values. Simulation is based on urban aerosol model over tropical atmosphere

irradiance at the top of atmosphere (TOA), $\tau_{\lambda,i}$ is the total optical depth of the ith scatterer or absorber, and m_i is the air mass of the ith scatterer or absorber through the atmosphere. Taking the natural logarithm of both sides, Eq. 2.25 can be written as

$$\ln I_\lambda = \ln R^2 I_{o,\lambda} - \sum \tau_{\lambda,i} m_i. \tag{2.26}$$

The total optical depth, $\tau_{\lambda,i}$ in Eq. 2.26 is contributed by Rayleigh, ozone, aerosol and trace gases, which can be written as

$$\tau_{\lambda,i} = \tau_{R,i} + \tau_{o,i} + \tau_{a,i} + \tau_{g,i}. \tag{2.27}$$

The Rayleigh contribution is approximated using the relationship (Djamila et al. 2011; Knobelspiesse et al. 2004)

$$\tau_{R,\lambda,i} \propto \frac{p}{p_o} \exp\left(-\frac{H}{7998.9}\right), \tag{2.28}$$

where p is the site's atmospheric pressure, p_o is the mean atmospheric pressure at sea-level and H is the altitude from sea-level in meter. Meanwhile, the ozone optical depth can be estimated through the satellite observation of ozone concentration, C_o in Dobson unit (DU) (Knobelspiesse et al. 2004)

$$\tau_{o,\lambda,i} \propto C_o. \tag{2.29}$$

Other major trace gases contributions are nitrogen dioxide and sulphur dioxide. These contributions are more dominant in highly urbanized or industrial area. Similarly, their optical depth can be estimated through the satellite observation or ground-based measurement of their respective concentration.

According to Eq. 2.26, the uncalibrated pixels (counts, P) measured by the spectrometer is then

$$\ln P_\lambda = \ln R^2 P_{o,\lambda} - \sum \tau_{\lambda,i} m_i, \tag{2.30}$$

where $P_{o,\lambda}$ is the extrapolated pixels intercept at zero air mass. When the range of interest is restricted in visible bands, the trace gases contributions can be neglected. In this way, the remaining contributions are now constrained to Rayleigh and ozone only. Substituting Eq. 2.27 into 2.30 gives the final equation as

$$\ln P_\lambda + \tau_{R,i} m_i + \tau_{o,i} m_i = \ln R^2 P_{o,\lambda} - \tau_{a,i} m_i. \tag{2.31}$$

Using this approximation, changes in Rayleigh optical depth due to pressure fluctuation and nominal ozone optical depth at each point is subtracted. Thus, leaving the left side of Eq. 2.31 insensitive to pressure variations and differences caused by ozone (Michalsky and Kiedron 2008). This step is important because small changes in pressure or ozone column during the observation can noticeably affect the extrapolated values.

On a clear day, a Langley plot gives a stable $P_{o,\lambda}$ for each wavelength when the data are extrapolated to TOA. With sufficient data of $P_{o,\lambda}$ on several clear days, an averaged $P_{o,\lambda(avg)}$ can be obtained using the following equation

$$P_{o,\lambda(avg)} = \frac{1}{n} \sum_{i=n}^{i} P_{o,\lambda,n}, \tag{2.32}$$

n is the number of Langley plots available for calibration. Accordingly, the calibration factor k, is obtained by dividing the averaged extrapolated values with the extraterrestrial constant. Finally, the calibrated irradiance measured by the spectrometer is determined by multiplying the pixels measured at the ground P_λ with the calibration factor k as (Slusser et al. 2000)

$$I_\lambda = P_\lambda k = \frac{P_\lambda \int P_{o,\lambda(avg)} F_\lambda d\lambda}{I_{o,\lambda} \int F_\lambda d\lambda}. \tag{2.33}$$

2.4 Historical Development of Langley Calibration Method

The Langley calibration method can be categorized into five types chronologically. The oldest method is the basic sunphotometry Langley method. This is then followed by circumsolar Langley method, cloud-screened Langley method, maximum value composite (MVC) Langley method, and comparative Langley method. Details of each method are elaborated in the following.

2.4.1 Basic Sunphotometry Langley Method

The diminution of light passing through the atmosphere was for the first time quantified by Pierre Bouguer in 1725 (Shaw 1983). This attenuation was found increasing exponentially to the evolution of optical path length and led to the establishment of the well known Beer-Lambert-Bouguer's principle of exponential. For a thin layer of atmosphere, it could be considered as planar and therefore the passage of light through a pane of colored glass could be used to explain the mechanism of the transmission. In both mechanism, the optical transmission T obeys

$$T = \exp\left(\frac{-\varphi l}{\cos z}\right), \tag{2.34}$$

where l is the thickness of the medium, z is the angle of the beam of primary illumination, and ϕ is the optical index of the medium, which in this case is the turbidity optical index.

The determination of T in Eq. 2.34 is difficult as the primary incident illumination is inaccessible. Therefore, Eq. 2.34 should be considered in terms of an arbitrary reference at two angles of primary illumination Z_1, and $Z_{2,}$ then the ratio is given as

$$\ln(I_1/I_2) = \beta l[1/\cos z_1 - 1/\cos z_2], \tag{2.35}$$

where I represents the solar or lunar light intensity which is independent of I_o (the extraterrestrial solar light intensity) and the quantity βl is the quantity to be determined. In the case of glass plate, l is the thickness of the medium. However, in the atmosphere it represents the total optical path length travelled by I. This principle when used in Langley plot can be used to determine the instrument's output at TOA, which is useful in calibration for AOD retrieval. However, one important task in Langley calibration is to insure the temporal drifts in atmospheric transmissivity do not lead to erroneous calibration constants (Shaw 1983). The only way to achieve this is to perform the Langley calibration from an excellent high altitude mountain observatory.

2.4.2 Circumsolar Langley Method

Not long after that, a modified Langley calibration was developed, in which simultaneous measurements of circumsolar radiation are incorporated (Tanaka et al. 1986). In this method, the logarithm of the sunphotometer reading is plotted against the ratio of intensity of singly scattered circumsolar radiation to that of direct solar radiation instead of the optical air mass as in the conventional Langley method. The idea of using circumsolar radiation for monitoring atmospheric turbidity is based on the availability of the data of circumsolar radiation for quantitative detection of very small amounts of aerosols and other particulates and of small changes in their concentration, size and composition.

The single-scattering approximation of the circumsolar (aureole) intensity in the almucantar of the sun is given by

$$F_a^1(\mu_o, \varphi) = m\tau\omega_o P(\cos\theta) F_o \exp(-m\tau)\Delta\Omega, \tag{2.36}$$

where μ_o is the cosine of the solar zenith angle, ϕ is the azimuthal angle measured from the solar principal plane, ω_o is the single scattering albedo, $P(cos\theta)$ is the normalized phase function at the scattering angle θ, $\Delta\Omega$ is the solid viewing angle of the radiometer, and $cos\theta$ is given by

$$\cos\theta = \mu_0^2 + (1 - \mu_0^2)\cos\varphi. \tag{2.37}$$

From Eq. 2.36, the intensity of singly scattered radiation in the solar almucantar is proportional to the optical depth m_T contributed by aerosols and air molecules given by

$$\tau_T = \tau_a + \tau_m, \tag{2.38}$$

$$\omega_o = (\omega_{oa}\tau_a + \omega_{om}\tau_m)/\tau, \tag{2.39}$$

$$P(\cos\theta) = [\omega_{oa}\tau_a P_a(\cos\theta) + \omega_{om}\tau_m P_m(\cos\theta)]/\omega_o\tau, \tag{2.40}$$

where τ_a, ω_{oa}, and $P_a(cos\theta)$ are the optical depth, the single scattering albedo and the phase function of aerosols, respectively; and τ_m, ω_{om}, and $P_m(cos\theta)$ are corresponding quantities for air molecules. The phase function $P(cos\theta)$ is defined to satisfy the normalization integral of

$$2\pi \int_{-1}^{1} P(\cos\theta) d\theta = 1. \tag{2.41}$$

When simultaneous measurement of the intensity of direct solar radiation and that of circumsolar radiation from a given portion of the aureole region is made by a single radiometer, Eqs. 2.36–2.40 can be combined to form

$$\ln F = \ln F_o - \tau^*, \tag{2.42}$$

$$\tau^* = m\tau = F_a^1/[F\Delta\Omega\omega_o P(\cos\theta)]. \tag{2.43}$$

Given that the magnitudes of *P(cosθ)* are more or less independent of the size distribution of aerosols at scattering angle around 20°, the intensity of singly scattered radiation F_a^I from the measured intensity F_a by can be determined as

$$F_a^1 = SSR(m, \tau_a, \tau_m, \overline{m}, \omega, \theta)F_a, \tag{2.44}$$

where *SSR* is the single scattering ratio that depends on several parameters such as optical air mass m, optical depth of aerosols τ_a and air molecules τ_m, complex index of refraction of aerosol $\overline{m}$, ground albedo ω, and scattering angle θ.

Figure 2.6 presents an example of the modified Langley plot for turbidity condition of $\tau_a = 0.2$ at noon. The three regression lines in Langley plot on the left panel are simulated based on Shaw's parabolic drift parameter assumed α to be 0, 0.011 and −0.011, corresponds to change of τ_a in 0, 10, and −10 % for 3 h around noon. It is evident from the figure that the Langley-plot method predicts the symmetrically larger or smaller values of F_o for finite values of α despite of an excellent linearity in the respective plots. The circumsolar Langley method on the right panel improved the consistency and accuracy in 5–10 times for the wavelengths greater than 500 nm in spite of varying τ_a. Measurement of circumsolar radiation for the aureole-corrected Langley calibration had also been realized by pointing the observation direction to the side of the Sun instead of using theoretical circular aureole ring measurements (Nieke et al. 1999). Similar results were reported that inclusion of the aureole signal measurements significantly reduced the deviation compared to the classical Langley-plot analysis.

2.4.3 Cloud-Screened Langley Method

A sunphotometry Langley calibration particularly for the large network of automated instrument which collects large pool of data under both cloudless and non-cloudless condition needs to be cloud-screened prior to the calibration. For instance, the MFRSRs are usually operated in remote areas and unattended. Thus, their raw data represent a wide range of atmospheric conditions which may undesirable for AOD analysis when clouds obscure the sun. Moreover, MFRSRs are typically not calibrated against standard references and therefore must be calibrated in a relative way from their own measurement data (Augustine et al. 2003). Besides, a good cloud-screening algorithm should work on raw un-calibrated data as the use of the measurement's spectral signature for cloud screening can be affected by initial calibration uncertainties and thus results in ineffective cloud-screening. Owing to these issues, the Langley calibration method continued

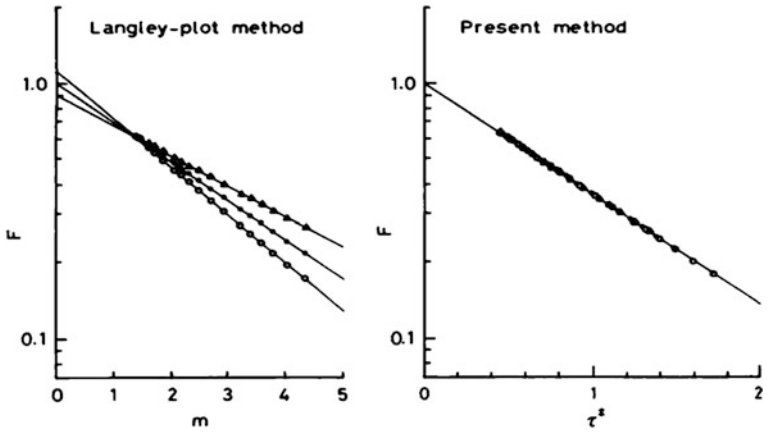

Fig. 2.6 Comparison between the Langley-plot method (*left panel*) and the Circumsolar Langley method (*right panel*) at $\lambda = 500$ nm (Tanaka et al. 1986)

to improve for an objective cloud-screening algorithm was introduced to select appropriate data from a continuous time series that needed for the regression.

2.4.3.1 Statistical Filters

The pioneer in this development was operating on a time series of direct normal irradiance observations, which can be described as a series of sequential filters that rejects undesirable points (Harrison and Michalsky 1994). In this method, the first filter is a forward finite-different derivative filter that identifies regions where the slope of Langley plot is positive. These cannot be produced by any uniform air mass turbidity process and are evidence of the recovery of the direct-normal irradiance from a cloud transits. The second filter is a subsequent finite-difference derivative filter tests for regions of strong second derivatives. In this case, regions that are more than twice the mean are eliminated. In other words, this filter rejects points near the edge of intervals eliminated by the first filter, if it was insufficiently aggressive, and also eliminates any cloud passage that occurs at the end of the sampling interval. To further affect a robust linear regression, two iterations are imposed by performing a conventional least-square regression on the remaining points from each filtration and a sweep is made through data points that have more than 1.5 standard deviation from the regression line or residual less than 0.006.

An example that demonstrates the Langley regression for the morning interval identified by the objective algorithm is presented in Fig. 2.7. In the figure, the points marked with "+" contribute equally to the regression and points marked with small open box were removed by the derivative filters in the time-series plot near AM = 2.0. The first iteration removes a weak cloud passage in the time-series plot around AM = 4.5. These points are marked with a box and cross. The

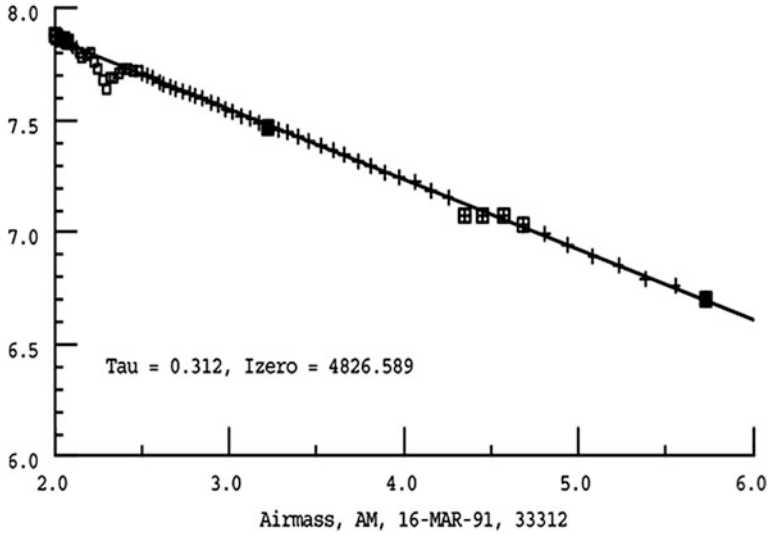

Fig. 2.7 Objective cloud-screening algorithm imposed in Langley calibration $\lambda = 500$ nm (Harrison and Michalsky 1994)

second iteration removes two points marked with a solid black box. Though these would not symmetrically affect the regression if retained, this second iteration is important if the data are noisier. At a difficult site, this method can provide a free long-term stability test for the instrument and permit the instrument calibration to be tied to solar output.

2.4.3.2 Clear-Sky Detection Algorithm

The concept of using statistical filter in Langley-plot as constrain for data selection is limited only for true clear-sky condition. In particular, under fictitious clear-sky conditions that are unable to be identified by the statistical filter, large inaccuracies may incur in the Langley extrapolation as part of the cloudy or aerosol-contained data will be used as guidance in the filtration process. Unlike the statistical-filtered Langley method that based on the simple minded notion of using least square regression on all available data, the clear-sky detection algorithm in Langley-plot uses only clear-sky condition data for the calibration analysis. In this way, the selection is completely automated and independent of the true clear-sky condition on a single day of observation.

One of the most popular algorithms used in Langley calibration is the Long and Ackerman clear-sky detection algorithm (Augustine et al. 2003). The algorithm uses four sequential tests that scrutinize total solar and diffuse solar irradiance to detect cloud-free skies. These tests hypothesize that cloudy and hazy skies exhibit characteristics in the components of down-welling shortwave irradiance that clear

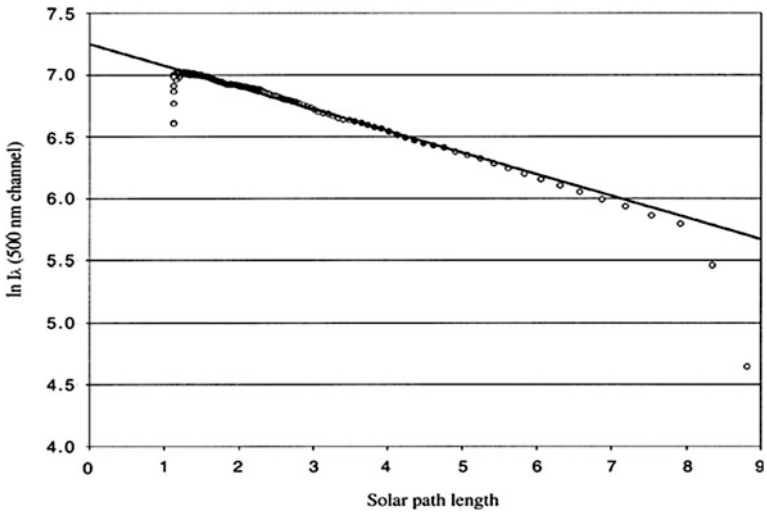

Fig. 2.8 Langley plot for the MFRSR 500 nm channel. *Solid circles* represent time periods identified as clear by Long and Ackerman clear-sky detection algorithm (Augustine et al. 2003)

skies do not. The first two tests eliminate periods of obvious cloudiness by comparing normalized transformation of the total and diffuse solar measurements to expected clear-sky limits. The other two tests examine temporal variations of parameters computed from the total and diffuse solar irradiance to further remove subtle periods of thin cloud or hazy conditions for more confident clear sky condition.

An example of a Langley plot for the MFRSR 500 nm channel at Table Mountain SURFRAD station the morning of 23 Apr 2001 is adapted from Augustine et al. (2003) given in Fig. 2.8. The solid circles represent time periods identified as clear by the Long and Ackerman (2000) method and the line is the least squares linear fit to the solid (clear sky) points only. The resultant $I_{o,\lambda}$ calibration value was applied to two Asian dust-related high air pollution events and the results suggested that error of retrieval is $\pm 0.01 \pm 0.05$, depending on the solar zenith angle. Though this method had been shown useful for selecting periods of MFRSR data appropriate for Langley-plot calibration, it requires collocated independent broadband solar component measurement for the clear-sky determination particularly for nominally un-calibrated radiometer.

2.4.4 Maximum Value Composite (MVC) Langley Method

Quiet recently, a new solar Langley calibration method to derive AOD from MFRSR data under extremely hazy atmospheric condition was proposed (Lee et al. 2010). It involves the acquisition of the maximum value composite (MVC) of

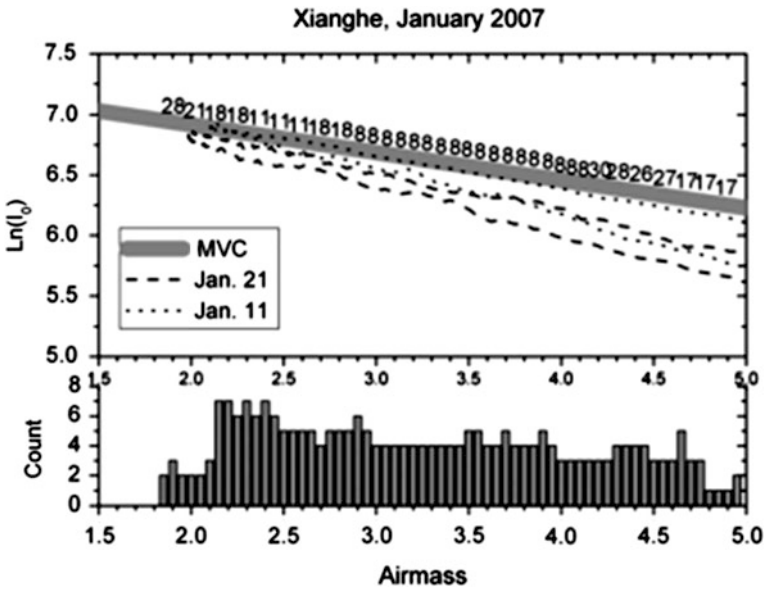

Fig. 2.9 Comparison between maximum value composite (MVC) Langley method and conventional Langley method at 500 nm channel (Lee et al. 2010)

the largest irradiance values at a given air mass. Regression of the Langley plot is based on these values because they can represent the clear-sky and minimum aerosol loading. Due to statistical uncertainties, not all maximum values can be used. Anomalous values such as zero or abnormally large/small values are removed by screening out local minima/maxima. This is performed by comparing values in neighboring air mass bins from which a standard deviation of relative difference of <1 % is removed.

Figure 2.9 shows the maximum value composite (MVC) result at 500 nm for one month of period and conventional Langley plots of single day within the month in dotted and dashed line (Lee et al. 2010). Histogram represents the number of days contributing to the MVC Langley method. All three resultant regression lines have high correlation coefficient >0.99 but different in y-intercept which represents the calibration value. Differences in I_0 by MVC regression and by single day Langley plots lead to large error (0.01 $\sim$ 0.40) in AOD determination. When compared to the AERONET method, results from MVC Langley method are comparable and within the acceptable error of <0.02 (Lee et al. 2010). However, one major shortcoming of this method is the MVC method cannot deal with temporal changes in extrapolated value of Langley-plot during a given composite period. To be specific, if the period of time is too long, information about the temporal variability is lost and if it is too short, there may be a dearth of valid data.

2.4.5 Comparative Langley Method

The comparative Langley method basically works in a recalibration basis by comparing to a well-calibrated wavelength or extrapolated value for improved calibration constant. Unlike the four previously described methods, this method does not perform the calibration experimentally instead it improves the calibration constant intrinsically through recalibration that based on presumed constant.

2.4.5.1 Ratio Estimation

It is a comparative calibration method which depends on a known calibration of a reference wavelength to permit calibration at the other wavelengths by assuming the relative size distribution of aerosol to remain constant as (Arai and Liang 2011)

$$\tau_a(\lambda, t) = \pi M(t) \int K_{ext}(r, \lambda) f(r') d \ln r', \tag{2.45}$$

where *f(r')* is the relative size distribution that is dependent only on the particle radius *r'*, and *M(t)* is the multiplier necessary to produce correct size distribution at some time, *t*. In this way, the ratio of aerosol optical depth between different wavelengths is assured to be constant as

$$\tau_a(\lambda_1, t)/\tau_a(\lambda_2, t) = \tau_a(\lambda_1, t_o)/\tau_a(\lambda_2, t_o) = \psi. \tag{2.46}$$

Thus, calibration at other wavelengths is feasible using the reference wavelength that is assumed to be well-calibrated by

$$\ln P(\lambda_1) + m(\tau_m(\lambda_1) + \tau_o(\lambda_1)) = \ln P_o(\lambda_1) - \psi m \tau_a(\lambda_o), \tag{2.47}$$

where λ_0, λ_1 are the reference and calibrate wavelength, respectively.

By adopting the similar approach suggested by Arai and Liang (2011), the improved Langley method by ratio estimation is conducted in three processes, level 0, calibration and level 1. In the level 0, based on the reference wavelength, the AOD at other wavelengths are estimated using the wavelength dependent relationship as Eq. 2.47. In the calibration, P_o at each observation is retrieved using the estimated AOD from level 0. Finally, in the level 1, the measured pixel is calibrated into direct normal irradiance (DNI) in physical unit using the P_o value obtained in the calibration level. Thus, more accurate solution of AOD can be estimated by reanalysis of the calibrated volume spectrum using the absolute extraterrestrial constant obtained directly from reference solar spectrum at top-of-atmosphere.

2.4.5.2 Monte Carlo Approximation

This comparative Langley method implements a weighted Monte Carlo (MC) approximation to find an improved calibration by minimizing the diurnal variation in Angstrom's exponent α and its curvature γ (Kreuter et al. 2013). The method simulates a large ensemble of random combination of calibration constant weighted with a Gaussian uncertainty function centered on a mean constant, and selects the calibration constant that yields the smallest diurnal variations (DV). The AOD dependency on wavelength is usually described by Angstrom's power law as

$$\log \tau_a = \log \beta_\mu - \alpha \log \lambda, \tag{2.48}$$

with λ is the wavelength in microns, β_μ is the AOD at wavelength of one micron. To account for a possible curvature, it has become common to add a quadratic term in logarithm λ as

$$\log \tau_a = \log \beta_\mu * + \alpha \log \lambda - \gamma \log^2 \lambda. \tag{2.49}$$

The parameters α and γ are determined by regression of Eqs. 2.48 and 2.49, respectively. The idea of this method is to harness the sensitivity of parameter α and γ on derived AOD by minimizing any residual DV in α and γ. Since both α and γ show independent DVs, the total diurnal variation (TDV) amplitude to be minimized as

$$TDV^2 = DV_\alpha^2 + DV_\gamma^2. \tag{2.50}$$

Noted that using a random number for an erroneous calibration constant V'_o that is normally distributed is an implicit weighting of the solution by the mean square error of the absolute V_o and MC calibration constant V_{mc}. Therefore, smaller deviations of V'_o from V_o are more likely generated in the MC approximation. Thus the retrieval of AOD using V_{mc} should be found as close to V_o as possible. The method had been proven to reduce the calibration uncertainty by a factor of up to 3.6 (Kreuter et al. 2013). It may also be easily generalized to other sunphotometer with more aerosol wavelength channels to improve the calibration beyond the Langley uncertainty.

References

Alexandrov MD, Marshak A, Cairns B et al (2004) Automated cloud screening algorithm for MFRSR data. Geophys Res Lett 31:L04118. doi:10.1029/2003GL019105

Arai K, Liang XM (2011) Comparative calibration method between two different wavelengths with aureole observations at relatively long wavelength. Int J Appl Sci 2:93–101

Augustine JA, Cornwall CR, Hodges GB et al (2003) An automated method of MFRSR calibration for aerosol optical depth analysis with application to an Asian dust outbreak over the United States. J Appl Meteorol 42:266–278

Bohren CF, Huffman DR (1983) Scattering by particles. Absorption and Scattering of Light by Small Particles

Che H, Zhang X, Chen H et al (2009) Instrument calibration and aerosol optical depth validation of the China Aerosol Remote Sensing Network. J Geophys Res 114:D03206. doi:10.1029/2008JD011030

Djamila H, Ming CC, Kumaresan S (2011) Estimation of exterior vertical daylight for the humid tropic of Kota Kinabalu city in East Malaysia. Renew Energy 36:9–15

Dubovik O, Holben B, Eck TF et al (2002) Variability of absorption and optical properties of key aerosol types observed in worldwide locations. J Atmos Sci 59:590–608

Dubovik O, King MD (2000) A flexible inversion algorithm for retrieval of aerosol optical properties from Sun and sky radiance measurements. J Geophys Res 105:20673–20696

Dubovik O, Smirnov A, Holben BN (2000) Accuracy assessments of aerosol optical properties retrieved from AERONET Sun and sky-radiance measurements. J Geophys Res 105:9791–9806

Harrison L, Michalsky J (1994) Objective algorithms for the retrieval of optical depths from ground-based measurements. Appl Opt 33:5126–32

King MD, Byrne DM, Herman BM, Reagan JA (1978) Aerosol size distributions obtained by inversion of spectral optical depth measurements. J Atmos Sci 35:2153–2167

Knobelspiesse KD, Pietras C, Fargion GS et al (2004) Maritime aerosol optical thickness measured by handheld sun photometers. Remote Sens Environ 93:87–106

Kreuter A., Wuttke S, Blumthaler M (2013) Improving Langley calibrations by reducing diurnal variations of aerosol Ångström parameters. Atmos Meas Tech 6:99–103. doi:10.5194/amt-6-99-2013

Lee KH, Li Z, Cribb MC et al (2010) Aerosol optical depth measurements in eastern China and a new calibration method. J Geophys Res 115:1–11. doi:10.1029/2009JD012812

Michalsky JJ, Kiedron PW (2008) Comparison of UV-RSS spectral measurements and TUV model runs for clear skies for the May 2003 ARM aerosol intensive observation period. Atmos Chem Phys 8:1813–1821. doi:10.5194/acp-8-1813-2008

Mie G (1908) Contributions to the optics of turbid media particularly of colloidal metal solutions. Ann Phys 330:377–445

Nieke J, Pflug B, Zimmermann G (1999) An aureole-corrected Langley-plot method developed for the calibration of HiRES grating spectrometers. J Atmos Solar-Terrestrial Phys 61:739–744

O'Neill NT, Eck TF, Holben BN, Smirnov A, Dubovik O, Royer A (2001) Bimodal size distribution influences on the variation of angstrom derivates in spectral and optical depth space. J Geophys Res Atmos 106:9787–9806

Schmid B, Wehrli C (1994) High precision of calibration of a sun photometer using Langley plots performed at Jungfraujoch (3580 m) and standard irradiance lamps. Geoscience and Remote Sensing Symposium 1994. IGARSS'94. Surface and Atmospheric Remote Sensing: Technologies, Data Analysis and Interpretation. International. pp 2314–2316

Shaw GE (1983) Sunphotometry. Bull Am Meteorol Soc 64:4–10

Slusser J, Gibson J, David B et al (2000) Langley method for calibrating UV filter radiometer. J Geophys Res 105:4841–49

Smirnov A, Holben BN, Eck TF et al (2000) Cloud-screening and quality control algorithms for the AERONET database. Remote Sens Environ 73:337–349

Smirnov A, Holben BN, Giles DM et al (2011) Maritime aerosol network as a component of AERONET–first results and comparison with global aerosol models and satellite retrievals. Atmos Meas Tech 4:583–597

Tanaka M, Nakajima T, Shiobara M (1986) Calibration of a sunphotometer of direct-solar and circumsolar by simultaneous radiations measurements. Appl Opt 25:1170–1176

Thomason LW, Herman BM, Reagan JA (1983) The effect of atmospheric attenuators with structured vertical distributions on air mass determinations and Langley plot analysis. J Atmos Sci 40:1851–1854

http://www.springer.com/978-981-287-100-8

Ground-Based Aerosol Optical Depth Measurement Using Sunphotometers

Dayou, J.; Chang, J.H.W.; Sentian, J.

2014, VI, 62 p. 21 illus., 10 illus. in color., Softcover
ISBN: 978-981-287-100-8